Crack propagation mechanisms in plain woven CFRP

A focus on intralaminar fracture under mixed-mode loading

Ruivo Fuga, Felipe; Monticeli, Francisco Maciel; Donadon, Maurício Vicente; Cândido, Geraldo Maurício

DOI
10.1016/j.tafmec.2025.105039

Publication date
2025

Document Version
Final published version

Published in
Theoretical and Applied Fracture Mechanics

Citation (APA)
Ruivo Fuga, F., Monticeli, F. M., Donadon, M. V., & Cândido, G. M. (2025). Crack propagation mechanisms in plain woven CFRP: A focus on intralaminar fracture under mixed-mode loading. *Theoretical and Applied Fracture Mechanics*, *139*, Article 105039. https://doi.org/10.1016/j.tafmec.2025.105039

Theoretical and Applied Fracture Mechanics 139 (2025) 105039

Contents lists available at ScienceDirect

Theoretical and Applied Fracture Mechanics

journal homepage: www.elsevier.com/locate/tafmec

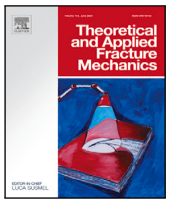

Crack propagation mechanisms in plain woven CFRP: A focus on intralaminar fracture under mixed-mode loading

Felipe Ruivo Fuga [a,*], Francisco Maciel Monticeli [b], Maurício Vicente Donadon [a], Geraldo Maurício Cândido [a]

[a] Departamento de Engenharia Aeronáutica, Instituto Tecnológico de Aeronáutica (ITA), Praça Marechal Eduardo Gomes, 50, Vila das Acácias, São José dos Campos, SP, Brazil

[b] Department of Aerospace Structures and Materials, Faculty of Aerospace Engineering, Delft University of Technology, Delft, The Netherlands

ARTICLE INFO

Keywords:
Fracture mechanics
Mixed-mode fracture
Intralaminar damage
Composite materials
Contour integral analysis
Phenomenological fracture criterion

ABSTRACT

The design of damage-tolerant aeronautical composite structures often involves thin-walled components that are susceptible to in-plane mixed-mode fracture. Unlike with metals, this process is complicated by the composites anisotropy and the lack of standardized procedures for predicting failure in notched, holed or cracked composites under mixed-mode loading. This study introduces a novel Modified Arcan Fixture (MAF) for testing Compact Tension Shear (CTS) specimens of carbon fibre woven reinforced polymer composite. Digital Image Correlation (DIC) was used to capture strain fields and calculate Stress Intensity Factors (SIFs), which were then compared to analytical predictions for different mode combinations and notch lengths. R-curves were generated for specimens exhibiting self-similar crack propagation. The results revealed that failure modes were dominated by tensile cracking in Mode I and compressive cracking in Mode II, indicating that a single-parameter fracture criterion inadequate for the failure description. A theoretical model that incorporates both tensile and compressive cracking is proposed, which can accurately predict the complete mixed-mode fracture envelope. Furthermore, Scanning Electron Microscopy (SEM) and X-ray micro-tomography were used to elucidate the mechanisms of surface failure and the morphology of internal damage.

1. Introduction

The growing use of composite materials demands accurate prediction of crack propagation to design reliable, lightweight damage tolerant structures. Aviation industry has shown that minimizing structural weight reduces fuel consumption and operational costs in aviation, therefore resulting in thinner structures, where the plane stress condition assumption is valid. However, the heterogeneous nature of composites requires different approaches to the cracking phenomena as cracks can propagate in different materials in different propagation modes. Cracking in composites is commonly categorized into two primary mechanisms: interlaminar cracking, where cracks propagate along the matrix interface between plies, and intralaminar cracking, where cracks extend through both the matrix and the fibres within a single ply. This terminology is adopted throughout this work, consistent with [1–4]. However, many authors [5–8] also suggest the translaminar fracture nomenclature for through-the-thickness cracking.

Several studies have addressed interlaminar cracking under mixed-mode, including accurate finite element procedures as in [8–13]. In contrast, a comprehensive understanding of the effects of fibre orientation, specimen size, and fixture configuration on intralaminar cracking under mixed-mode loading is not yet fully established for composite materials. Singular stress and strain fields for isotropic materials have been extensively studied as in Williams [14] and Erdogan and Sih [15], while fracture criteria have been proposed through a combination of SIFs such as Maximum Tangential Stress (MTS) and Strain Energy Density (SED) [16,17]. A comprehensive review on isotropic criteria is presented in Wang et al. [18]. Complex variable solution method proposed by Lekhnitskii [19] followed by [20–23] extended the singular stress field description based on SIFs for the anisotropic case.

Experiments on mixed fracture in glass fibre unidirectional composites were performed by Wu [23], resulting in an empirical relation between SIF's to describe fracture. Buczek and Herakovich [21] and Gregory and Herakovich [22] proposed a Maximum Normal Stress Ratio criterion for composite materials, where the maximum tangential stress is compared to the material strength in the corresponding direction. In this criterion an elliptical tensile strength envelope along

* Corresponding author.
E-mail addresses: fuga@ita.br (F. Ruivo Fuga), f.m.monticeli@tudelft.nl (F.M. Monticeli), donadon@ita.br (M.V. Donadon), geraldomcan@gmail.com.br (G.M. Cândido).

https://doi.org/10.1016/j.tafmec.2025.105039
Received 9 April 2025; Received in revised form 2 June 2025; Accepted 6 June 2025
Available online 23 June 2025

material directions was assumed. Carloni and Nobile [24] and Carloni and Nobile [25] extended this methodology incorporating the strain energy density as a criterion and applications under bi-axial planar load cases, respectively. Cahill et al. [26] performed static tests on a variety of specimens showing that cracks propagate parallel to the fibre direction in unidirectional composites. The author also implemented a through the extended finite element method an elliptical toughness envelope to represent the fracture criterion. For unidirectional composites, where a significant strength difference between orthogonal directions exists, the criterion provides a simple yet robust method for predicting crack growth direction. However, when strength values along both orthogonal material directions do not differ significantly, as in the case of plain weave composites, the validity of the aforementioned criteria are unknown.

Experimental procedures for in-plane fracture in composite laminates is also a relevant research subject, as no standard method is yet available. One methodology consists of modifications on the loading fixture proposed by Arcan et al. [27], where mixed-mode plane stress is enforced on specimens, referred to as Modified Arcan Fixtures (MAFs). Conversely to the ASTM rail shear test [28], MAFs displays the potential of ranging from pure opening to pure sliding fracture modes, using the Compact Tension Shear (CTS) and V-notched specimens, for instance. MAF applications for composite mixed mode fracture testing are presented in [29–36]. Laffan et al. [37] introduced a mixed mode compact tension specimen for Uni-Directional (UD) IM7/8552 fibre reinforced composites, representing a variation on CTS proposed by Richard and Benitz [38]. For a cross-ply laminate under opening modes, fibre fracture was the dominant failure characteristic, while matrix cracks and delamination was expressive under sliding fracture modes displaying increasing R-curves. Boyina et al. [31] performed in-plane mixed-mode tests on plain weave glass fibre composites using a CTS specimen with loading angles of 0°, 22.5° and 45°. Load–displacement curves showed an increase in non-linearity as the mixed-mode ratio increased. Similarly to Laffan et al. [37], a compliance calibration method was used to calculate R curves under mixed-mode. Jamali et al. [39] showed that for UD E-glass under sliding modes a hackle pattern is formed, in which matrix cracks develop along the specimen, increasing the total energy dissipation. Using the same material, Gan et al. [33] adapted a V-notched specimen configuration from ASTM D7078 [28], so that a uniform shear stress could be applied under Mode II and concluded that the failure envelope could be determined using Puck's criterion for UD composites. Moreover, Digital Image Correlation Techniques (DIC) were employed, allowing for the *in-situ* evaluation of strain-fields. Hao et al. [40] also used DIC and a V-notched specimen to evaluate strains on twill reinforced carbon composites. The use of DIC led to the conclusion that non-linear in-plane shear behaviour plays an important role, as a great extent of distortion occurs and the fibres become misaligned. A comparison between E-glass, Kevlar and Carbon woven fabrics using a MAF was conducted by Taghibeigi et al. [41]. Fracture envelopes were generated using the compliance calibration method, obtained through linear elastic analysis using finite elements. This methodology was expanded by Zeinedini et al. [42] for cotton/epoxy laminates where a fracture envelope was proposed by adjusting the criterion parameters to the experimental data. Applications of a MAFs are also reported in [42–44] where finite geometry effects on the SIF were accounted for.

A systematic review of experimental characterization of mixed mode fracture for the intralaminar cracking on composite materials is presented in [45] showing that one of the key factors motivating the use of the Compact Tension Shear (CTS) configuration is its ability to minimize deformation originating from regions of the specimen unrelated to the crack tip altering its toughness, as addressed by [46]. Potential undesired failure mechanisms include longitudinal compressive stresses on the face opposite the crack tip, compressive stresses on the upper and lower specimen surfaces, in-plane shear stresses, compressive stresses at the hole edges, shear stresses between the holes and the specimen edges, and specimen buckling, [3,47]. To accurately assess these damage modes, digital image correlation (DIC) analysis must be supplemented by fractographic examination using scanning electron microscopy (SEM) and X-ray microtomography (micro-CT), since some internal damage features cannot be detected by conventional microscopic techniques [48].

This paper introduces a new MAF design that allows for CTS specimens to be tested under in-plane mixed-mode fracture conditions, with dimensions comparable to the ASTM E399 [49] standard for Mode I loading. During the tests, different failure mechanisms and cracking characteristics were observed. Fractographic characterization was conducted through Scanning Electron Microscopy and micro Computer Tomography revealing that for Mode I load cases, tensile failure resulted in self-similar crack extension. However, curved crack extension paths were obtained for specimens under mixed-mode, specially when loaded at a 45° angle. For sliding fracture modes, compressive failure was the dominant cracking mechanism. Strain fields processed through the DIC technique during the tests were compared to analytical predictions, in terms of first order approximation using SIFs. A novel fracture initiation criterion was formulated in terms of the local stress evaluation using SIFs (K_I and K_{II}), describing cracking due to both tensile and compressive failures. The proposed formulation was confronted to existing fracture criteria, showing that the complete fracture envelope could be modelled through a phenomenological framework. Lastly, from the experimental data, the relationship between applied load and crack length was established, and R curves generated. This study contributes to the understanding of intralaminar crack propagation in composite materials, showcasing an experimental methodology capable of observing strain-fields throughout the tests. Moreover, the novel phenomenological fracture criterion based on a theoretical model provided valuable insights on the cracking mechanisms aiding the analysis and design of damage-tolerant composite structures.

2. Theoretical modelling

2.1. Stress field for plane stress anisotropic bodies

Stress field around an infinite, linear elastic, anisotropic body under mixed-mode load cases can be evaluated using Lekhnitskii's complex variable method solutions [19], as presented in [20–22,50].

$$\begin{Bmatrix}\sigma_{xx}(r,\theta)\\ \sigma_{yy}(r,\theta)\\ \tau_{xy}(r,\theta)\end{Bmatrix}=\begin{Bmatrix}\frac{K_I}{\sqrt{2\pi r}}Re\left[\frac{\mu_1\mu_2}{\mu_1-\mu_2}\left(\frac{\mu_2}{z_2}-\frac{\mu_1}{z_1}\right)\right]+\frac{K_{II}}{\sqrt{2\pi r}}Re\left[\frac{1}{\mu_1-\mu_2}\left(\frac{\mu_2^2}{z_2^2}-\frac{\mu_1^2}{z_1^2}\right)\right]\\ \frac{K_I}{\sqrt{2\pi r}}Re\left[\frac{1}{\mu_1-\mu_2}\left(\frac{\mu_2}{z_2}-\frac{\mu_1}{z_1}\right)\right]+\frac{K_{II}}{\sqrt{2\pi r}}Re\left[\frac{1}{\mu_1-\mu_2}\left(\frac{1}{z_2}-\frac{1}{z_1}\right)\right]\\ \frac{K_I}{\sqrt{2\pi r}}Re\left[\frac{\mu_1\mu_2}{\mu_1-\mu_2}\left(\frac{1}{z_2}-\frac{1}{z_1}\right)\right]+\frac{K_{II}}{\sqrt{2\pi r}}Re\left[\frac{1}{\mu_1-\mu_2}\left(\frac{\mu_2}{z_2}-\frac{\mu_1}{z_1}\right)\right]\end{Bmatrix}. \tag{1}$$

Eq. (1) shows the stress components for a global coordinate system xy for a point at distance r and direction θ in relation to the crack tip, where:

$$z_1 = cos(\theta) + \mu_1 sin(\theta). \tag{2}$$

$$z_2 = cos(\theta) + \mu_2 sin(\theta). \tag{3}$$

In Eqs. (2) and (3), μ_i are the roots of the characteristic polynomial representing the differential equation using the complex variable method (Eq. (4)). Coefficients a_{ij} are the effective elastic compliance tensor components evaluated along the crack coordinate system directions as shown in Fig. 1.

$$a_{11}\mu^4 - 2a_{16}\mu^3 + (2a_{12}+a_{66})\mu^2 - 2a_{26}\mu + a_{22} = 0. \tag{4}$$

Similarly, using the constitutive relation for a linear elastic aniso tropic material, strain fields can be obtained from Eq. (5). For orthotropic materials with material directions aligned with global coordinate system xy, the shear-extension coupling terms a_{16} and a_{26}, become

zero.

$$\begin{Bmatrix} \epsilon_{xx}(r,\theta) \\ \epsilon_{yy}(r,\theta) \\ \gamma_{xy}(r,\theta) \end{Bmatrix} = \begin{bmatrix} a_{11} & a_{12} & a_{16} \\ a_{12} & a_{22} & a_{26} \\ a_{16} & a_{26} & a_{66} \end{bmatrix} \begin{Bmatrix} \sigma_{xx}(r,\theta) \\ \sigma_{yy}(r,\theta) \\ \tau_{xy}(r,\theta) \end{Bmatrix}. \tag{5}$$

Magnitudes K_I and K_{II} in Eq. (1) represent global SIF's under mixed-mode. For a MAF, K_I and K_{II} are a function of the loading angle defined as β, [29,51–53]. Finite geometry effects are accounted for in the functions f_I and f_{II}. Eqs. (6) and (7) show the global SIF definitions for the MAF where w, t, a and F represent the lamina width, thickness, crack length and load, respectively. Finite geometry corrections f_I and f_{II} are also applicable for linear elastic anisotropic materials. However, for this approach the functions represent not only the finite geometry, but also anisotropy effects on SIF. Therefore, $f_I = f(a_{ij}, a/w)$ and $f_{II} = g(a_{ij}, a/w)$ with a/w representing the finite geometry contribution.

$$K_I = \frac{F cos(\beta)\sqrt{\pi a} f_I}{wt}. \tag{6}$$

$$K_{II} = \frac{F sin(\beta)\sqrt{\pi a} f_{II}}{wt}. \tag{7}$$

Additionally, as derived by Sih et al. [20] and discussed in Azhdari and Nemat-Nasser [54], strain energy release rates for each mode (G_I and G_{II}) can be calculated from the corresponding stress intensity factors (K_I and K_{II}) for an anisotropic body with compliance coefficients a_{ij}, as displayed in Eq. (8). Similarly to Eq. (1), linear elasticity under plane stress is assumed.

$$\begin{Bmatrix} G_I \\ G_{II} \end{Bmatrix} = \begin{Bmatrix} -K_I \frac{\sqrt{\pi}}{2} a_{22} Im\left[\frac{K_I(\mu_1+\mu_2)+K_{II}}{\mu_1\mu_2\sqrt{\pi}}\right] \\ K_{II} \frac{\sqrt{\pi}}{2} a_{11} Im\left[\frac{K_{II}(\mu_1+\mu_2)+K_I\mu_1\mu_2}{\sqrt{\pi}}\right] \end{Bmatrix}. \tag{8}$$

However, when dealing with composite material failure, stress components are commonly evaluated at the material directions defined by the 12 coordinate system. Eqs. (9) and (10) show stress components at material directions, as a function of the ply orientation angle α in relation to the crack directions (x, y) as displayed in Fig. 1. Similarly, tangential stress components can be evaluated by performing plane stress rotations on the global tensor components xy, for any given direction θ, as shown in Eq. (11).

$$\sigma_{11} = \cos^2(\alpha)\sigma_{xx} + \sin^2(\alpha)\sigma_{yy} + \sin(2\alpha)\tau_{xy}. \tag{9}$$

$$\sigma_{22} = \sin^2(\alpha)\sigma_{xx} + \cos^2(\alpha)\sigma_{yy} - \sin(2\alpha)\tau_{xy}. \tag{10}$$

$$\sigma_{\theta\theta} = \sin^2(\theta)\sigma_{xx} + \cos^2(\theta)\sigma_{yy} - \sin(2\theta)\sigma_{xy}. \tag{11}$$

2.2. Mixed-mode fracture criterion

In-plane crack extension under mixed-mode can be predicted by different criteria through combination of K_I and K_{II} in a scalar function that describes failure [55]. In the isotropic case, crack extension occurs at the maximum tangential stress [15] or maximum tangential strain [56] directions, which are related to the maximum SERR [57]. However, for composite laminae, strength and toughness might depend on orientation. Buczek and Herakovich [21] evaluated the ratio between stress and strength at a critical distance r_c for all θ, thus defining the crack extension direction. Similarly, criteria in terms of tangential or normal strains can be defined. The following proposed model takes into account the following assumptions:

- Tensile failure can lead to slant cracks at mixed-mode conditions;
- Compressive failure occurs along the fibre directions only.

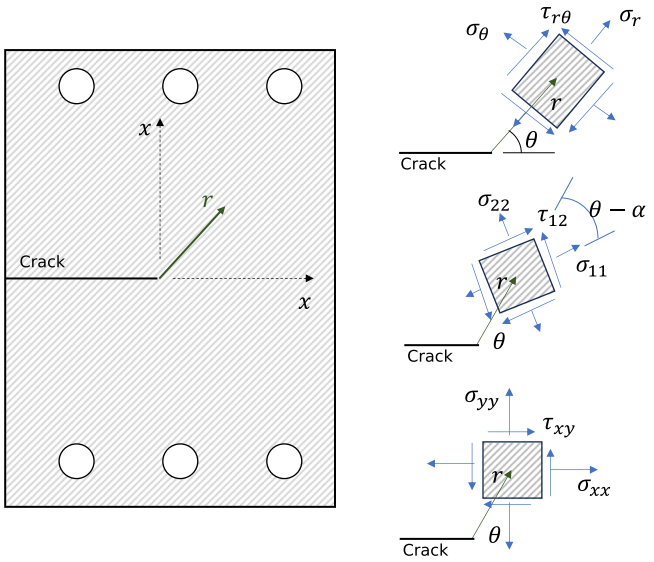

Fig. 1. Stress components at different orientations.

Fracture criterion can be expressed in terms of either material directions or tangential directions around the crack tip. Substituting Eq. (1) into Eq. (11), the tangential stress becomes as given in Box I.

The tensile failure criterion can be expressed in terms of a failure index presented in Eq. (15), where unstable propagation occurs at the critical angle where $f_\theta \geq 1$. Interestingly, distance r is not required for the failure evaluation. For the proposed model the toughness associated with tensile failure $K_c^t(\theta)$ is assumed as constant for the plain weave carbon fibre composite.

$$f_\theta(\theta) = \frac{\sigma_{\theta\theta}\sqrt{2\pi r}}{K_c^t} \text{ if } \sigma_{\theta\theta} > 0. \tag{15}$$

Conversely, compressive failure occurs along one of the material directions and is related to a micro-buckling that occurs in the reinforcement fibres, [58]. Therefore, the associated toughness is constant, for each direction θ and a failure index f_c is defined as in Eq. (16).

$$f_c(\theta) = \begin{cases} \frac{-\sigma_{11}\sqrt{2\pi r}}{K_c^c}, & \text{if } \sigma_{11} < 0 \\ -\frac{\sigma_{22}\sqrt{2\pi r}}{K_c^c}, & \text{if } \sigma_{22} < 0. \end{cases} \tag{16}$$

Critical SIF's under mixed-mode loading, expressed in Eqs. (6) and (7) can be computed at the corresponding critical loads and loading angle β for a MAF. These SIF components enable a mixed-mode failure envelope to be generated and confronted to the predicted failure criteria predictions displayed in Eqs. (15) and (16), where K_c^t and K_c^c are the input parameters.

2.3. Finite geometry effects for anisotropic materials

Finite geometry effects can be accounted for using finite element contour integral solutions for SIF's at different crack lengths. An in depth description of the SIF extraction procedure within finite elements was performed by Shih et al. [59]. In addition, Henshell and Shaw [60] and Barsoum [61] showed that the use of quadratic displacement interpolation for plane stress elements with mid side nodes positioned at 1/4 of the elements length is able to reproduce a singularity at the crack tip, with a $1/\sqrt{r}$ strain interpolation along the element boundaries. The use of quarter length mid-side nodes coupled with contour integral evaluation is currently implemented at the commercial finite element code *Abaqus/Standard*. Therefore, this procedure was employed for the specimen's geometry and stacking sequence. By prescribing the load F

$$\sigma_{\theta\theta}\sqrt{2\pi r} = K_I\left[\sin^2\theta\,\mathrm{Re}\left\{\frac{\mu_1\mu_2}{\mu_1-\mu_2}\left(\frac{\mu_2}{z_2}-\frac{\mu_1}{z_1}\right)\right\}+\cos^2\theta\,\mathrm{Re}\left\{\frac{1}{\mu_1-\mu_2}\left(\frac{\mu_1}{z_2}-\frac{\mu_2}{z_1}\right)\right\}-\sin(2\theta)\,\mathrm{Re}\left\{\frac{\mu_1\mu_2}{\mu_1-\mu_2}\left(\frac{1}{z_1}-\frac{1}{z_2}\right)\right\}\right]$$
$$+K_{II}\left[\sin^2\theta\,\mathrm{Re}\left\{\frac{1}{\mu_1-\mu_2}\left(\frac{\mu_2^2}{z_2}-\frac{\mu_1^2}{z_1}\right)\right\}+\cos^2\theta\,\mathrm{Re}\left\{\frac{1}{\mu_1-\mu_2}\left(\frac{1}{z_2}-\frac{1}{z_1}\right)\right\}-\sin(2\theta)\,\mathrm{Re}\left\{\frac{1}{\mu_1-\mu_2}\left(\frac{\mu_1}{z_1}-\frac{\mu_2}{z_2}\right)\right\}\right]. \quad (12)$$

Similarly, substituting Eq. (1) into Eqs. (9) and (10), the apparent SIFs along material directions become:

$$\sigma_{11}\sqrt{2\pi r} = K_I\left[\cos^2\alpha\,\mathrm{Re}\left\{\frac{\mu_1\mu_2}{\mu_1-\mu_2}\left(\frac{\mu_2}{z_2}-\frac{\mu_1}{z_1}\right)\right\}+\sin^2\alpha\,\mathrm{Re}\left\{\frac{1}{\mu_1-\mu_2}\left(\frac{\mu_1}{z_2}-\frac{\mu_2}{z_1}\right)\right\}+\sin(2\alpha)\,\mathrm{Re}\left\{\frac{\mu_1\mu_2}{\mu_1-\mu_2}\left(\frac{1}{z_1}-\frac{1}{z_2}\right)\right\}\right]$$
$$+K_{II}\left[\cos^2\alpha\,\mathrm{Re}\left\{\frac{1}{\mu_1-\mu_2}\left(\frac{\mu_2^2}{z_2}-\frac{\mu_1^2}{z_1}\right)\right\}+\sin^2\alpha\,\mathrm{Re}\left\{\frac{1}{\mu_1-\mu_2}\left(\frac{1}{z_2}-\frac{1}{z_1}\right)\right\}+\sin(2\alpha)\,\mathrm{Re}\left\{\frac{1}{\mu_1-\mu_2}\left(\frac{\mu_1}{z_1}-\frac{\mu_2}{z_2}\right)\right\}\right] \quad (13)$$

$$\sigma_{22}\sqrt{2\pi r} = K_I\left[\sin^2\alpha\,\mathrm{Re}\left\{\frac{\mu_1\mu_2}{\mu_1-\mu_2}\left(\frac{\mu_2}{z_2}-\frac{\mu_1}{z_1}\right)\right\}+\cos^2\alpha\,\mathrm{Re}\left\{\frac{1}{\mu_1-\mu_2}\left(\frac{\mu_1}{z_2}-\frac{\mu_2}{z_1}\right)\right\}-\sin(2\alpha)\,\mathrm{Re}\left\{\frac{\mu_1\mu_2}{\mu_1-\mu_2}\left(\frac{1}{z_1}-\frac{1}{z_2}\right)\right\}\right]$$
$$+K_{II}\left[\sin^2\alpha\,\mathrm{Re}\left\{\frac{1}{\mu_1-\mu_2}\left(\frac{\mu_2^2}{z_2}-\frac{\mu_1^2}{z_1}\right)\right\}+\cos^2\alpha\,\mathrm{Re}\left\{\frac{1}{\mu_1-\mu_2}\left(\frac{1}{z_2}-\frac{1}{z_1}\right)\right\}-\sin(2\alpha)\,\mathrm{Re}\left\{\frac{1}{\mu_1-\mu_2}\left(\frac{\mu_1}{z_1}-\frac{\mu_2}{z_2}\right)\right\}\right]. \quad (14)$$

Box I.

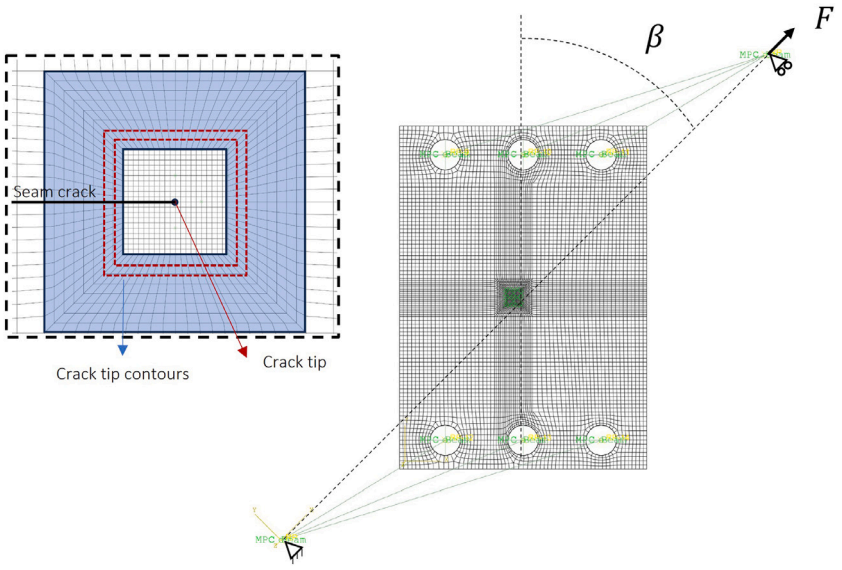

Fig. 2. Model mesh using plane stress shell elements and rigid bodies.

for the contour integral analysis, f_I and f_{II} expressions were obtained directly from Eqs. (6) and Eqs. (7), similarly to the procedure employed by Rikards et al. [29]. Multiple models were generated for different crack lengths under both Mode I and Mode II load cases. Fig. 2 shows the CTS specimen mesh, for a given load case, using 8-node plane stress shell elements (S8R). The crack is modelled as a region of nodes that do not share degrees of freedom, represented as a seam crack. For this analysis, the MAF was not modelled, as it was assumed a rigid body constraint for the external load, that is applied at an angle β in relation to the crack tip, shown in Fig. 2. Under this methodology finite geometry factors are a function of both geometry and material properties.

3. Experimental set-up

3.1. Specimen manufacturing

Compact Tension-Shear (CTS) specimens were manufactured by the Resin Transfer Molding process using a woven, plain weave, carbon fibre fabric (Hexcel® HexForce™ AGP193-P) and Huntsman Araldite® LY 5052 epoxy resin, mixed with Huntsman Aradur® 5052 hardener. A $[0]_{16}$ layup was used with an average laminate thickness of 3.84 mm, so that the effective compliance of the laminate could be analytically analysed as a single lamina, given that all plies share the same orientation. Frossard et al. [62] and Furtado et al. [4] showed that for thin unidirectional laminates the critical SERR increases approximately linearly with the ply thickness. However, throughout this study, the effects of different laminate thickness values were not addressed and all specimens share an average ply thickness of 0.24 mm. Cure cycle consisted of 24 h at room temperature, followed by a post cure cycle of 4 h at $100°C$. The same constituents and procedures were used for the specimens in Fuga and Donadon [63].

Mechanical characterization tests were performed for tensile and in-plane shear using ViC-Gauge image acquisition system so that strains could be computed using GOM Correlate DIC software. Tests were performed under displacement control using a ZwickRoell tensile testing machine EXMACRO-H02 with a 250 kN load cell. Table 1 shows the lamina material properties obtained from performed tests under

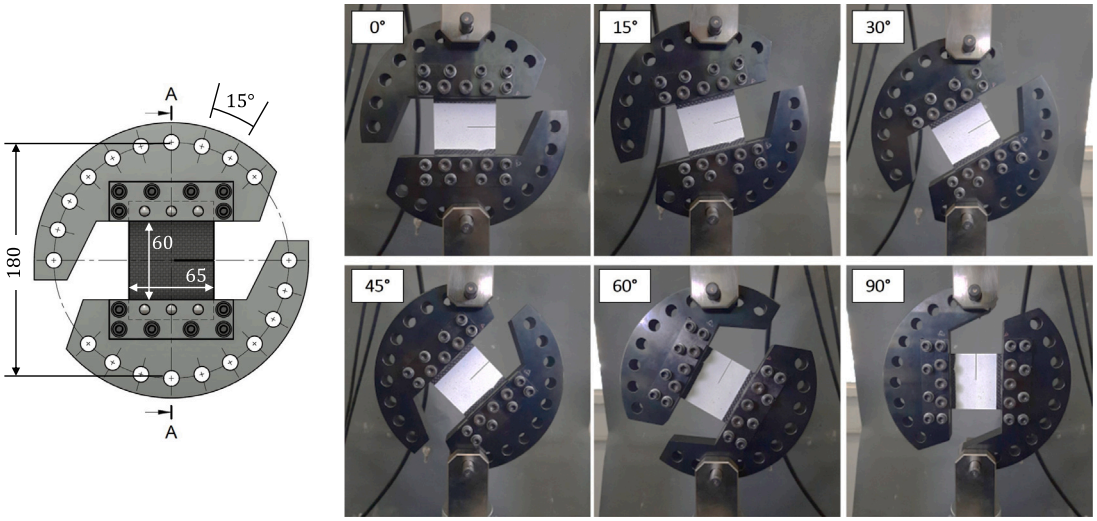

Fig. 3. CFRP specimen on Arcan device for mixed-mode fracture.

Table 1
Material properties for woven composite lamina.

E_{11} [GPa]	E_{11} [GPa]	G_{12} [GPa]	ν_{12}
58.64	58.64	2.57	0.06

ASTM standards [64,65]. CTS specimen were machined to the geometry displayed in Fig. 1. Notches of approximately 0.5 mm thickness were made using a circular saw, while the tip of the notch was sharpened using a razor blade. Specimens were loaded through three 8 mm holes. Two notch sizes were used, where the length $a_0 = 30$ mm is referred to CTS specimen, while the length $a_0 = 40$ mm is referred to as the CTSL, with the L in the acronym standing for the longer notch version. Both configurations share the remaining dimensions such as height, width and thickness, of 90 mm, 65 mm and 3.84 mm respectively.

3.2. Modified arcan fixture

A MAF was designed to provide in-plane mixed-mode fracture load cases, as shown in Fig. 3. The figure shows the CTS specimen loaded into 6 load cases, ranging from pure opening fracture at loading angle $\beta = 0°$ to pure sliding at $\beta = 90°$. The device was manufactured from a quenched 4340 steel alloy and allows for mixed-mode conditions for $\Delta\beta = 15°$ steps. A 100kN capacity MTS hydraulic testing machine was used with the standard fracture mechanics clevis grips (Model 640) under displacement control.

To evaluate strains and crack position during the tests, the experimental testing set-up shown in Fig. 4(a) was used where a Video Gauge data acquisition system (Imetrum) records a video file synchronized with load and displacement data from the MTS machine. Video gauge system output allows for calculation of displacements, rotations and strains using a point-tracking algorithm. Additionally, video file enables frames to be exported and analysed using DIC GOM Correlate software, so that the strain field can be visualized as field variable. Crack length evolution was monitored by visual inspection through triggering of a crack marker. Imprinted scales were positioned on the specimen as displayed in Fig. 4(a). A DSLR camera connected to a monitor provided an enhanced view of the crack length scale for accurate crack measurements. Fig. 4(b) shows the load, displacement and crack marker outputs for a representative specimen under mode I fracture.

3.3. SEM and micro-CT analysis

Scanning electron microscopy (SEM) analyses were performed to characterize the fracture surfaces. To perform this analysis, the characterized failure region in each tested specimen was previously coated with a thin layer of gold ions by the sputtering process in a Quorum Q150R ES equipment. The observation and interpretation of the physical aspects resulting from failure via crack propagation were performed using a TESCAN scanning electron microscope model VEGA 3 XMU. Imaging was conducted using an acceleration voltage of 5–10 keV.

X-ray microtomography (micro-CT) analyses were performed to investigate/localize internal damage and crack morphology. These analyses were conducted using a Tomography imaging parameters were 0.4x objective lens, 160 kV/10 W source settings, 3 μm pixel size ensuring a nominal resolution of 9 μm, 3D spatial resolution with a complete scan cycle of 1000 projections, exposure time of 2 s, detector resolution of 1024 x 1024. The equipment used was the XRADIA (currently C. ZEISS), model Xradia Versa XRM - 510, and a micro-computed tomography scanner (FINEP process n° 01.12. 0150.00).

4. Results

4.1. Finite geometry functions

Finite geometry effects for the proposed layup are displayed in Fig. 5 for crack lengths of 30 mm to 55 mm, at 5 mm steps. Results showed a similar trend when compared to the isotropic finite geometry solutions proposed by [66] for acrylic (plexiglass) specimens. For mode I loading, a similar behaviour is expected as the laminate Poisson's ratio approaches zero and $E_{11} = E_{22}$. However, for mode II the orthotropic material displays a reduced shear modulus G_{12} when compared to the isotropic counterpart, resulting in lower SIFs.

Dashed lines represent the fitted expression for finite geometry effects on CTS specimen, for this specific layup configuration, and expressed in Eqs. (17) and (18).

$$f_I\left(a_{ij}, \frac{a}{w}\right) = \frac{1}{1-\frac{a}{w}}\left(0.4972e^{0.029a}\right). \tag{17}$$

$$f_{II}\left(a_{ij}, \frac{a}{w}\right) = \frac{1}{1-\frac{a}{w}}\left(-2.4(10^{-4})a^2 + 6.8(10^{-3})a + 0.657\right). \tag{18}$$

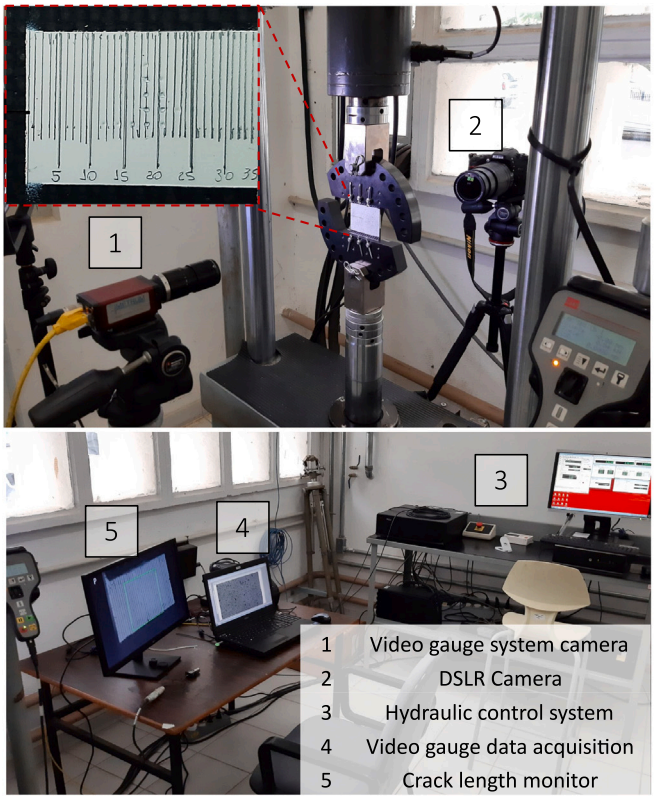

(a) Experimental set-up

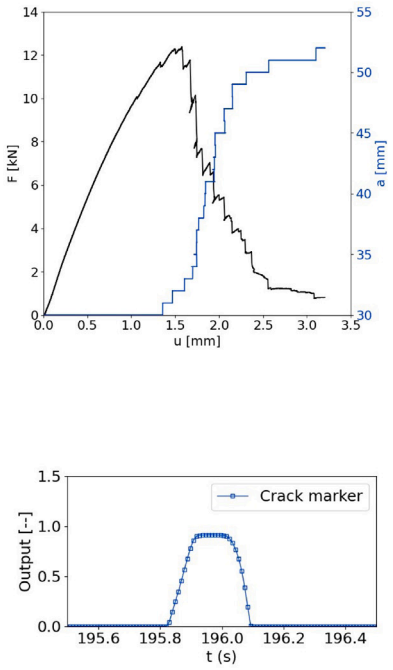

(b) Acquired data - load, displacement and crack position

Fig. 4. Experimental setup and data acquisition.

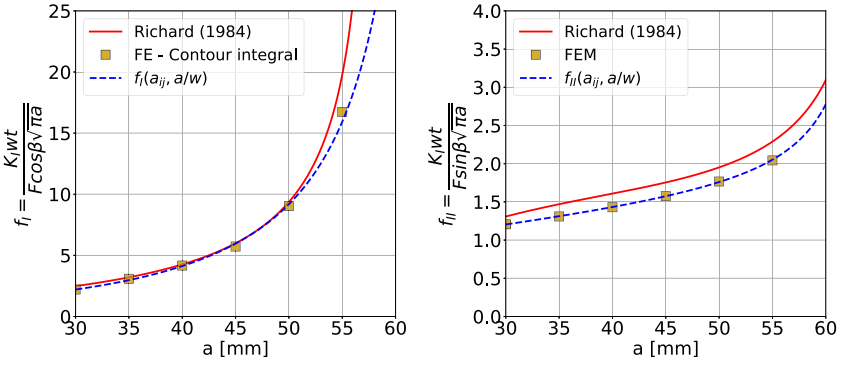

Fig. 5. Finite geometry and anisotropy effects.

4.2. Load–displacement data

Load–displacement data are shown in Fig. 6 for CTS and CTSL specimens with only one of the two specimens for each loading configuration displayed. For both notch sizes, fracture followed by complete separation occurred for loading angles (β) between 0° and 45° only, while specimens loaded at 60° and 90° showed multiple cracks and distortion. A non-linear behaviour in terms of load and displacements was observed as β increased. Despite the brittle behaviour of carbon epoxy laminates, the dissipation of micro cracks before a critical load is pronounced for shear dominated scenarios leading to a progressive energy dissipation, as discussed in [31,41,67]. Fig. 6 also shows the relation between maximum load for each specimen configuration and β as well as the relation between normal and tangential load components.

Crack propagation direction and failure modes are displayed in Fig. 7, for both specimen configurations. In the image, laminates are painted with a speckle pattern due to the DIC requirements for strain processing. Specimens loaded with $\beta \leq 30°$ displayed an approximately self-similar extension. For $\beta = 45°$ an initial inclination on the crack path was observed for both CTS and CTSL. Experimental results suggests that initial crack extension occurs at an angle, until a critical value from which crack propagation follows one of the orthotropy directions. For loading $\beta \geq 60°$, cracking due to compressive failure was observed, as displayed by the green arrows. From the images it is clear that

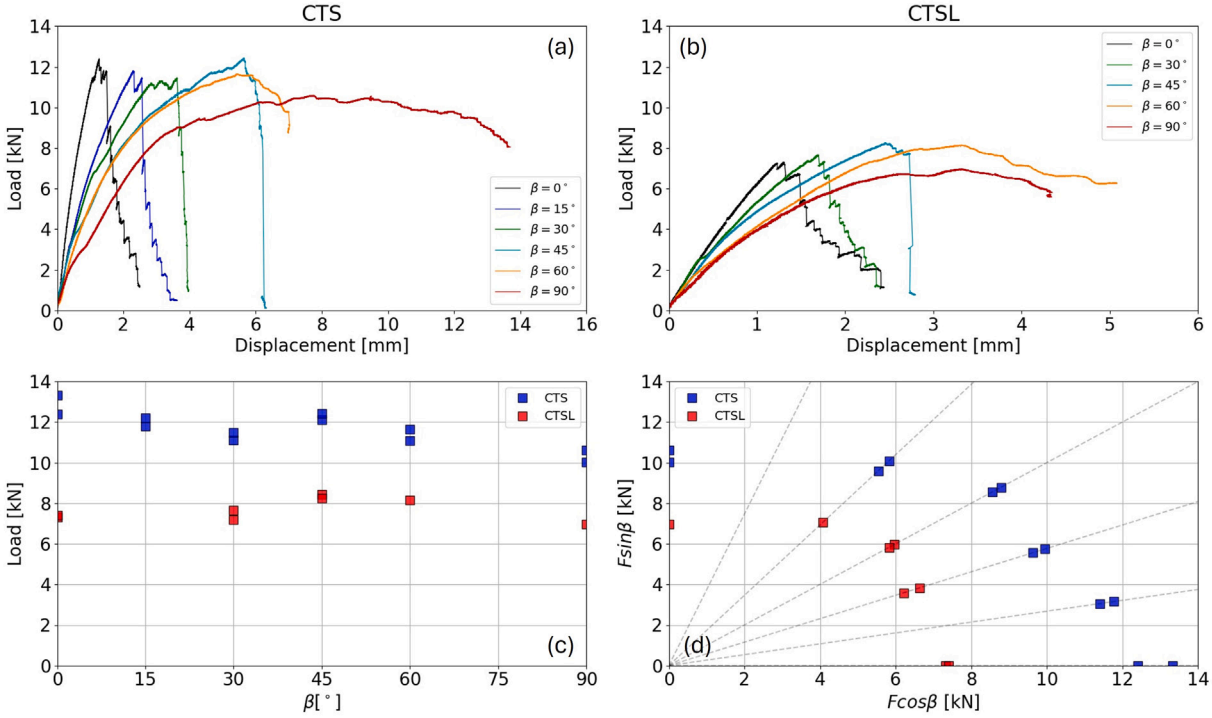

Fig. 6. Maximum load envelopes.

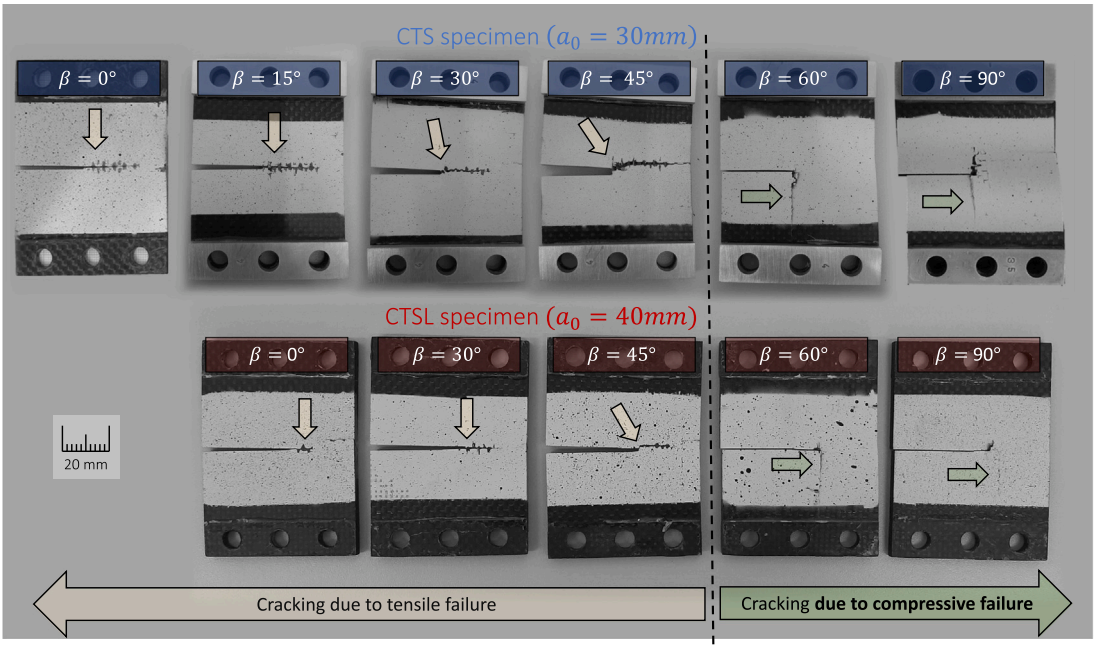

Fig. 7. Failure modes for CTS and CTSL specimens.

compressive failure showed a crack path aligned with the woven fibre orientation (vertical).

4.3. Strain fields — DIC

Evolution of normal strains as the crack propagates is displayed in Fig. 8, for the CTSL specimen under mode I. DIC plots show that strains along material direction 1 are concentrated at the crack tip as the crack advances.

Strain field under mixed-mode conditions were also generated. Fig. 9 shows principal strain for all six load cases, for the CTS specimen. Maximum principal strains are displayed, so that the combination of all tensor components can be easily visualized in a single variable. Due to the in-plane shear compliance, maximum principal strain fields are directly dependent to the shear strain magnitudes. The image also shows the correlation of experimental DIC strain data with analytical solutions, using Eq. (5) and the corresponding SIFs from Eqs. (6) and (7) and that analytical predictions are able to account for the orthotropic effects of the laminate. Strain fields are displayed for CTS specimens,

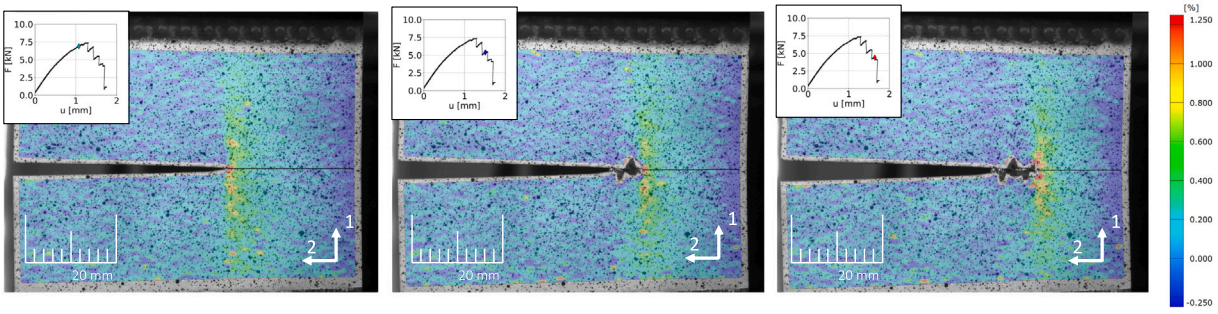

Fig. 8. Normal strain field evolution under Mode I – CTSL specimen.

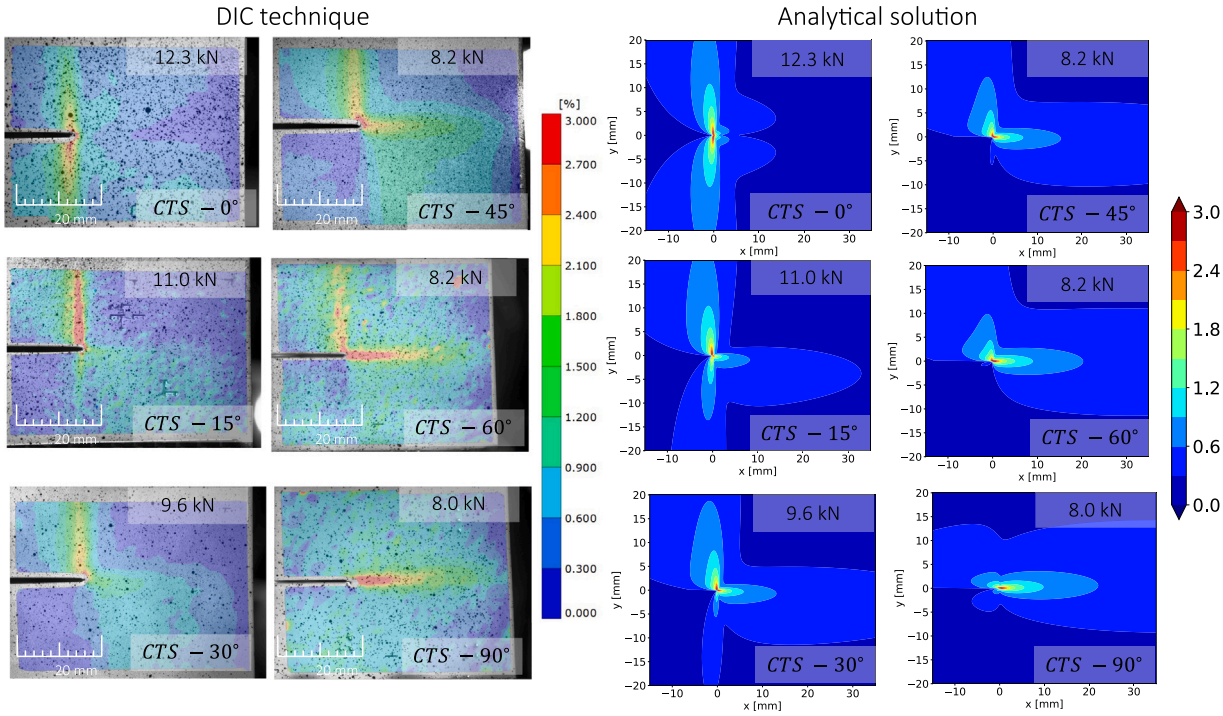

Fig. 9. Principal strain fields at different load angle β ($a_0 = 30$ mm).

however a similar profile is obtained for the CTSL configuration, with changes in strain magnitudes only.

Normal strain ϵ_{11} for points along a line in the original notch direction were plotted as a function of distance r for $\beta = 0°$, 30° and 45°, at 3kN and 9kN loads, for specimen CTS (Fig. 10). These angles are displayed, as the normal strain magnitudes are greater for mode I dominated load cases. Under the assumption of linear elasticity and at the vicinity of the crack tip (SIF dominated region), the opening strain profile predicted by Eq. (5) displays a good correlation to the experimental profile, therefore indicating that a SIF based fracture criterion could be established.

4.4. R curves

Load cases with $\beta \leq 45°$ were used to generate R curves, as an approximately self-similar condition was obtained. Resistance at mixed-mode was evaluated assuming a combination of SIFs evaluated at the load values that crack extension was observed, Eq. (19). The equivalent mixed-mode fracture toughness for tensile failure K_c^t displayed is only valid for conditions where orthotropy directions are aligned with the crack path for a self-similar crack extension. This is a direct result of the evaluation of strain energy release rate from Eq. (8) with $G_{Ic} = G_I + G_{II}$. Furthermore, for the toughness K_c^t expression to be obtained, data on the load, crack length and finite geometry factors are needed.

$$K_c^t(a) = \sqrt{K_I^2(F,a) + K_{II}^2(F,a)} \tag{19}$$

Fig. 11 show that for mode I, crack extends at a critical SIF of approximately $K_c^t = 1050$ MPa$\sqrt{mm}$ for the CTS and $K_c^t = 1300$ MPa$\sqrt{mm}$ for the CTSL. However, as the mixed-mode condition is introduced, a rising R-curve is observed. Similarly, Fig. 11 shows the resistance in terms of the SERR.

Although a detailed characterization of fracture toughness and R-curves under mixed-mode loading is not available for the same woven carbon fabric material system, the present study reports toughness values that are consistent with those found in multiple publications from the same research group [63,68,69]. Specifically, the reported mode I fracture toughness values (K_{I_c}) are 1582.4 MPa$\sqrt{\text{mm}}$, 1260.4 MPa$\sqrt{\text{mm}}$, and 1331.8 MPa$\sqrt{\text{mm}}$, respectively, calculated from the critical strain energy release rate using Eq. (8). In addition, a comparison between average toughness values for composite materials reported on the scientific literature is found at Monticeli et al. [45].

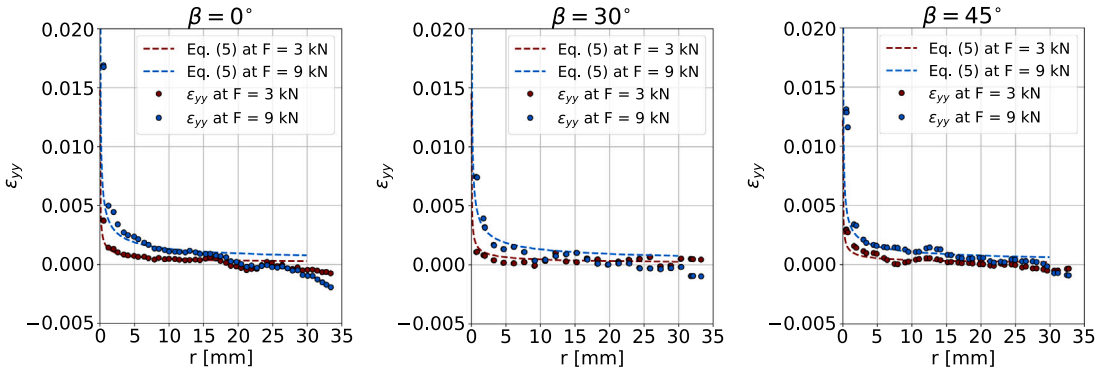

Fig. 10. Opening strain for a line along the notch direction — CTS.

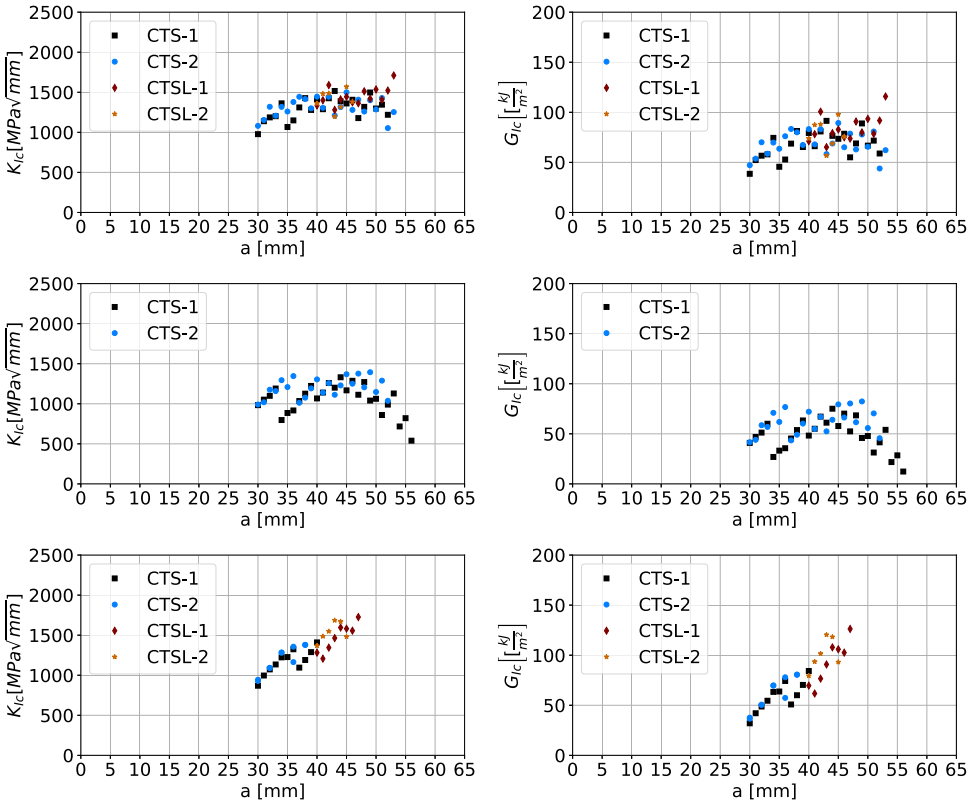

Fig. 11. R curves for CTS and CTSL specimens with $\beta < 45°$.

4.5. Fractographic analysis

Fig. 12 shows a Scanning Electron Microscopy (SEM) image with a 35x magnification for specimens loaded at β = 0°, 45° and 90°. Fibre breakage is the dominant failure aspect for specimens loaded in pure mode I, resulting in self-similar crack propagation. For β = 45°, cracking initial direction is not collinear with the notch, rather it develops an alternating pattern of failure along the local material directions 1 and 2, resulting in the path displayed in Fig. 7. Arrows in yellow represent the predicted crack extension direction using the novel fracture criterion, further discussed in Section 4.6. Under mode II loading, β = 90°, cracking due to compressive failure was initially observed. As the specimen was subjected to further deformation, tensile failure cracks were also observed, as indicated in Fig. 12.

Fractographic analyses were first carried out on specimens tested in the CTS configuration in Mode I (0°), Mixed Mode (45°) and Mode II (90°). Fig. 13 shows the three-dimensional reconstruction and corresponding sections of the top view (XY view) and side view (XZ view) of the fracture. It can be seen that the crack has passed through all layers without any geometric effect. There is a tendency to follow the fibre architecture, as can be seen in Fig. 12, where the fracture often occurs above or below the plane of propagation for transverse fibre fractures. This is due to the vertical fracture at the fibre/weft matrix interface (90°) being blocked by the warp (0°) and concentrating the tension for fibre fracture, causing fibre stretching and subsequent fracture and abrupt decay of the force reactions. The broom pattern observed in Figs. 12 and 13 and in cross-ply laminates is derived from the degree of ply splitting that occurs before fibre breakage. For the laminate subjected to pure shear (Fig. 13c), the internal regions of the material show compression in the vertical direction below the crack and tensile failure at 90° in the upper part of the crack. A series of delamination layers caused by deformation can also be observed in the region in front of the crack. There are also delamination layers in the compression region

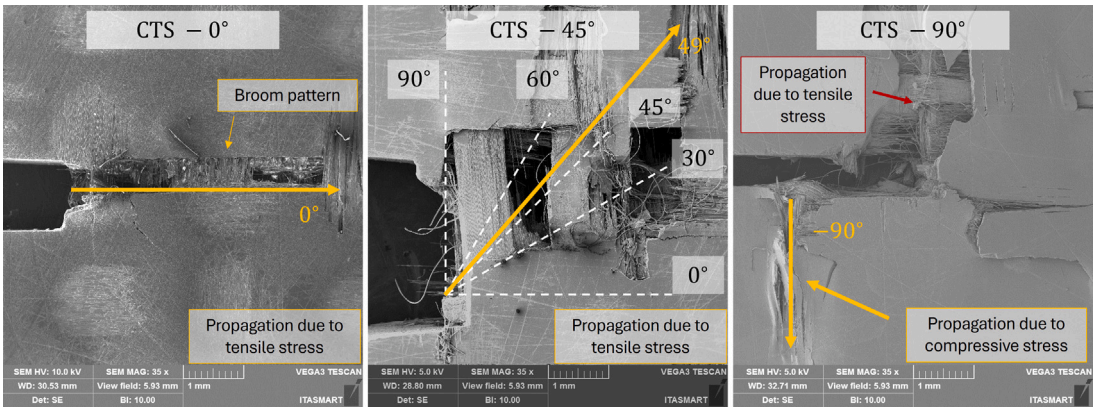

Fig. 12. SEM for CTS specimen with $\beta = 0°, 45°$, and 90°.

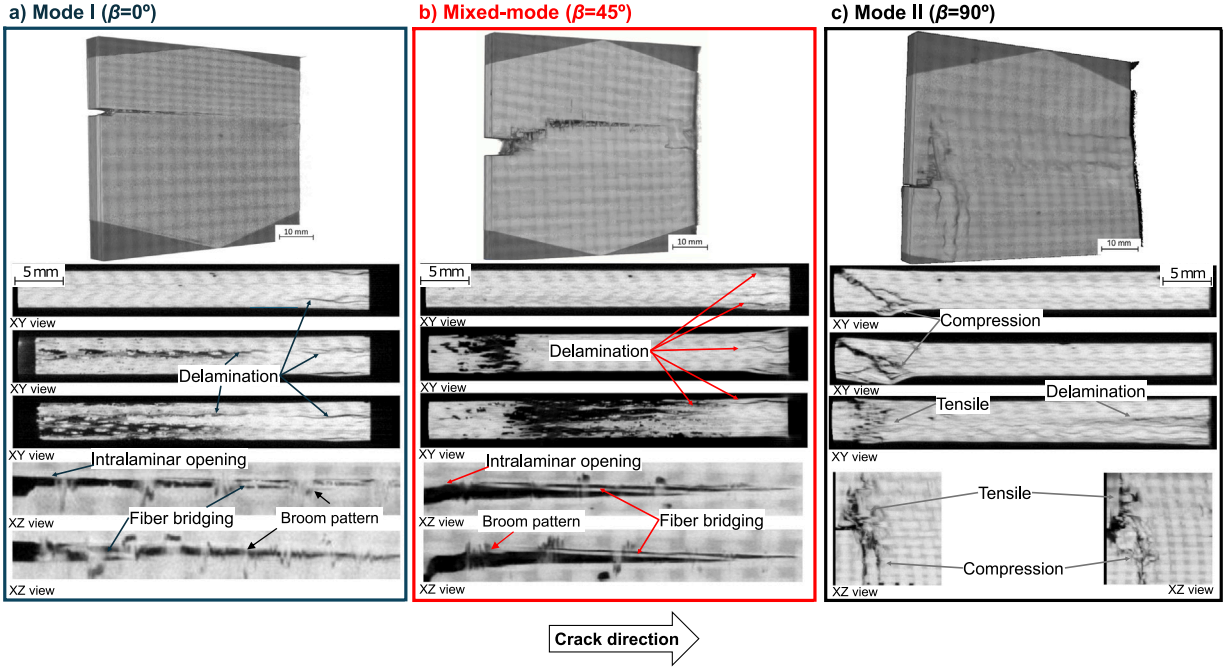

Fig. 13. Micro-CT of CTS specimen with $\beta = 0°$, 45°, and 90°.

(opposite the crack tip). In some cases, this damage mechanism was very close to both fronts, making it difficult to accurately control the influence of compressive stress for more extensive crack lengths.

4.6. Proposed fracture criterion predictions

Fig. 14 shows the predictions for the proposed fracture criterion assuming toughness values of $K_c^t = 1050$ MPa$\sqrt{mm}$ and $K_c^c = 2300$ MPa$\sqrt{mm}$ for the CTS specimen and $K_c^t = 1300$ MPa$\sqrt{mm}$ and $K_c^c = 2300$ MPa$\sqrt{mm}$ for specimen CTSL. In the image, dashed lines represent the maximum load until fracture due to tensile failure $f_\theta = 1$, while dotted lines show the corresponding results for compressive failure $f_c(\theta) = 1$. Maximum load for each load case is assumed as the minimum load value between the two criteria. Proposed model indicates that for specimens loaded with $\beta \leq 50°$, tensile failure is expected for both notch sizes, while for $\beta > 50°$, compressive failure is the dominant failure mechanism, as observed experimentally. Furthermore, crack initial propagation direction for tensile failure increases with loading angle, until the compressive failure limit, from which point cracks propagate at the direction $\theta = -90°$. Additionally, the maximum load for different mixed-mode conditions displayed a good correlation with experimental data using the fracture toughness parameters obtained from the R-curves.

Finally, the proposed fracture initiation criteria predictions were compared to other methodologies applicable to anisotropic materials. Fig. 15 shows the corresponding SIFs combinations under mixed-mode that lead to fracture initiation. Experimental data were obtained using Eqs. (6) and (7) at the maximum load condition. MTS, SED and RIS stand for Maximum Tangential Stress, Strain Energy Density and Reinforced Isotropic Solid criteria.

From the image it is clear that the introduction of a constant fracture toughness parameter for tensile failure $K_c^t(\theta)$ in Eq. (15) recovers the MTS criterion for anisotropic materials. However, it is important to express that the MTS criterion shown takes into account material anisotropy on the stress field, differently from the MTS criterion applied to isotropic materials. Similarly, the RIS model, proposed by Fakoor and Khezri [70] and Khaji and Fakoor [71], where stress tensor components are scaled according to the level of anisotropy and isotropic fracture initiation criteria are employed on the corresponding stress fields, is unable to represent compressive failure under mode II. Finally, minimum SED criterion for anisotropic materials, was plotted over experimental data. With the exception of the proposed criterion, other

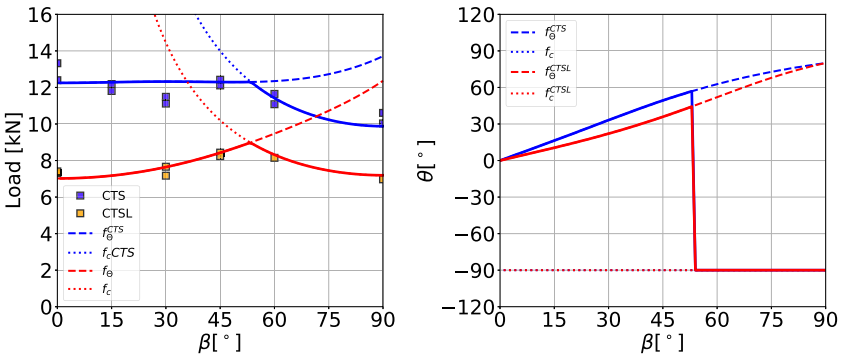

Fig. 14. Proposed mixed-mode fracture criterion predictions.

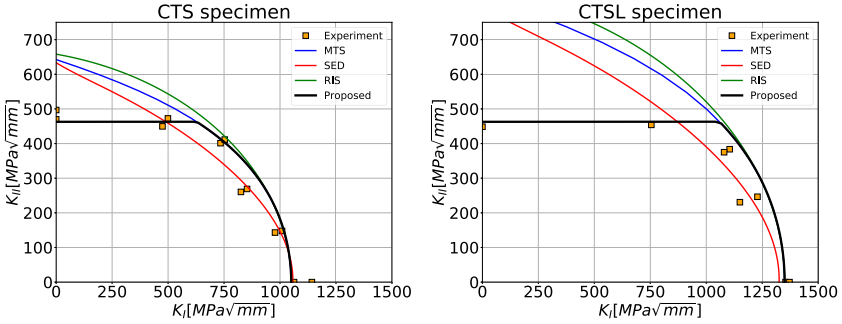

Fig. 15. Fracture initiation envelopes.

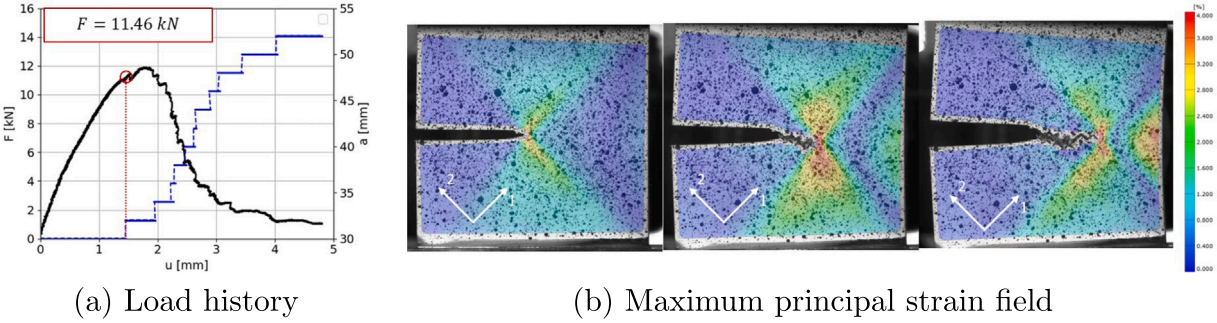

Fig. 16. Experimental data on ±45° laminate under Mode I.

envelopes fail to describe fracture under mode II loading for the tested specimen configurations, as different failure mechanisms occur. Therefore, a single toughness, strain energy density or strain energy release rate parameter is not sufficient to describe the complete envelope. The proposed criterion allows for different failure mechanisms to be accurately predicted, as shown by the correlation with experimental data. Moreover, the proposed criterion includes a stress description definition, which is commonly used to evaluate failure in composite materials in terms of local coordinates. Interestingly, SED criterion coupled with anisotropic stress field description provided a better correlation with experimental data on scenarios with tensile failure, indicating that the proposed methodology can be derived into a SED criterion with multiple parameters as well.

4.7. Off-axis laminate

A final validation of the proposed model was used for a mode I load case on a CTS specimen with off-axis stacking sequence(±[45°]). Fig. 16 shows the load–displacement data for the tested specimen, as well as the principal strain field plot for three different stages of propagation.

Assuming the same fracture toughness value for the CTS specimen $K_c^t = 1050$ MPa $\sqrt{mm}$ coupled with the finite geometry factor for this layup $f_I = 2.53$, obtained through FE contour integral analysis, a critical load of 10.7kN was predicted. With respect to the experimental value of 11.5kN, the error is within 7%. In addition, the analytical principal strain profile at the maximum load, Fig. 17(b), also correlates with experimental strain-field from Fig. 16.

Interestingly, the proposed model predicted a self-similar crack extension, as the maximum tangential stress occurs at $\theta = 0$, as shown in Fig. 17(a). SEM showed the alternating pattern between weft and warp fibre fracture under mode I for the off-axis laminate, as shown in Fig. 18, with a self-similar crack extension on the macro scale.

5. Conclusions

This paper investigated failure mechanisms associated with notched woven reinforced composite laminates under in-plane mixed mode loading. Firstly, the characterization of the strain field using DIC techniques showed that stress and strain field intensity can be accurately represented with a $(1/\sqrt{r})$ function at the vicinity of the crack tip. Furthermore, using finite element contour integral analysis, the finite

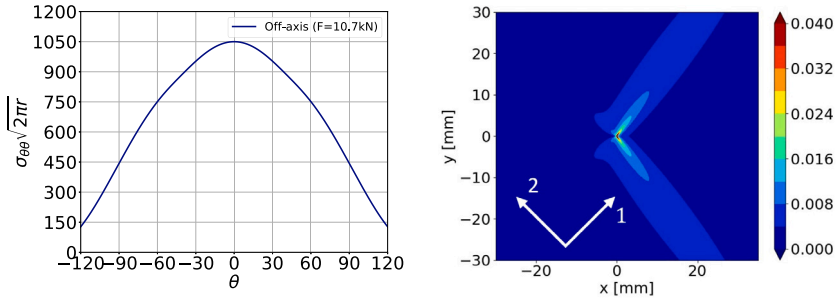

(a) Tangential stress intensity distribution (b) Maximum principal stress plot

Fig. 17. Analytical results for ±45° laminate under Mode I.

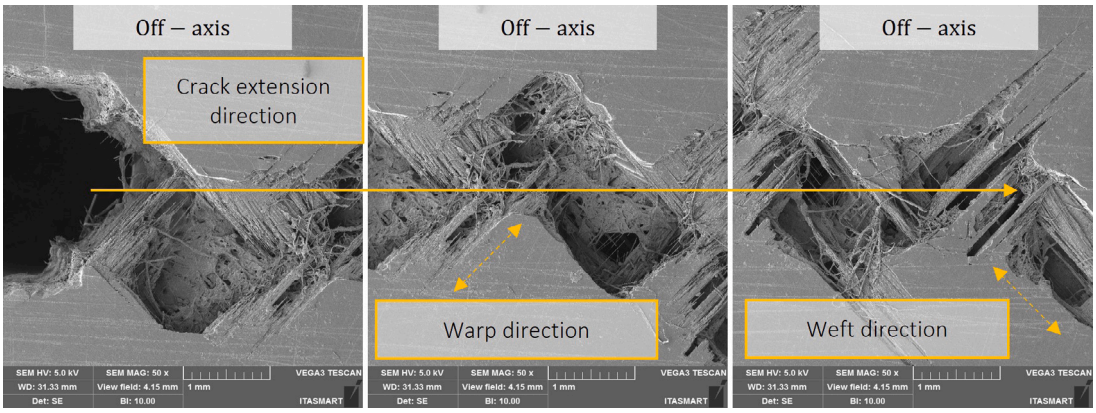

Fig. 18. SEM for off-axis specimen under Mode I loading.

geometry and corresponding stress intensity factors, provided a good correlation between measured and analytical strain fields for mixed-mode applications. Following the stress and strain-field description, loads required for crack extension were evaluated using the testing methodology and a novel theoretical fracture initiation criterion. Experimental results showed that for fracture modes dominated by mode I failure, cracks propagated in a quasi self-similar form. Differently, for mode II dominated load cases, compressive failure along the fibre direction was observed, perpendicular to the notch. For some mixed-mode conditions ($\beta = 45°$) specimens showed a curved crack path, displaying an alternating pattern of tensile failure along material directions. The proposed criterion, coupling tensile and compressive failure, resulted in a model that can accurately predict the maximum load capacity and describe inclined crack propagation directions at mixed-mode fracture. Finally, for specimens where the effect of initial crack direction are negligible ($\beta < 45°$), R-curves were generated under the assumption of a self-similar crack evolution. Tensile toughness of $K_c^t = 1050$ MPa$\sqrt{mm}$ and $K_c^t = 1300$ MPa$\sqrt{mm}$ were obtained for the specimens. Regarding compressive failure, a toughness of $K_c^c = 2300$ MPa$\sqrt{mm}$ was used to describe failure along the fibre directions in both specimens.

This research allowed for the description of different failure mechanisms on woven composites due to the different testing procedures employed. The choice of specimen configuration, coupled with the designed MAF and the use of DIC techniques led not only to the strain field correlation but also R-curves and fracture initiation envelopes to be generated. In addition the use of Micro-CT and SEM contributed to the physical description of failure mechanisms. From these in-depth analysis a novel physically based fracture criterion was proposed. Overall, the results of this study improve the understanding of mixed mode fracture in plain weave CFRP laminates, with particular relevance to the design and assessment of thin-walled composite structures under planar stress conditions.

Finally, this paper introduces a novel methodology for the description of fracture in anisotropic materials under mixed-mode, through the evaluation of stress fields at different directions. The authors recommend future research to be carried out on the extension of such criterion introducing different physically based failure criteria into a SIF description for the fracture locus under mixed-mode as in uni-directional composites or multi-directional layups for example.

CRediT authorship contribution statement

Felipe Ruivo Fuga: Writing – original draft, Validation, Investigation, Formal analysis, Data curation. **Francisco Maciel Monticeli:** Writing – review & editing, Visualization, Investigation, Data curation. **Maurício Vicente Donadon:** Writing – review & editing, Supervision, Project administration, Funding acquisition, Conceptualization. **Geraldo Maurício Cândido:** Writing – review & editing, Visualization, Resources, Investigation, Data curation.

Declaration of competing interest

The authors declare that they have no known competing financial interests or personal relationships that could have appeared to influence the work reported in this paper.

Acknowledgements

This study was financed in part by the Coordenação de Aperfeiçoamento de Pessoal de Nível Superior - Brasil (CAPES) - Finance Code 001 - Process No. 88887.489658/2020-00, PNPD/CAPES Process No. 88887.360818/2019-00, CNPq Grant No. 301069/2019-0 and CNPq Process No. 1736838/2023-6.

Data availability

Data will be made available on request.

References

[1] S. Jose, R. Ramesh Kumar, M.K. Jana, G. Venkateswara Rao, Intralaminar fracture toughness of a cross-ply laminate and its constituent sub-laminates, Compos. Sci. Technol. 61 (8) (2001) 1115–1122, http://dx.doi.org/10.1016/S0266-3538(01)00011-2.

[2] M.F.S.F. de Moura, R.D.S.G. Campilho, A.M. Amaro, P.N.B. Reis, Interlaminar and intralaminar fracture characterization of composites under mode I loading, Compos. Struct. 92 (1) (2010) 144–149, http://dx.doi.org/10.1016/j.compstruct.2009.07.012.

[3] N. Blanco, D. Trias, S.T. Pinho, P. Robinson, Intralaminar fracture toughness characterisation of woven composite laminates. Part II: Experimental characterisation, Eng. Fract. Mech. 131 (2014) 361–370, http://dx.doi.org/10.1016/j.engfracmech.2014.08.011.

[4] C. Furtado, A. Arteiro, P. Linde, B.L. Wardle, P.P. Camanho, Is there a ply thickness effect on the mode I intralaminar fracture toughness of composite laminates? Theor. Appl. Fract. Mech. 107 (2020) 102473, http://dx.doi.org/10.1016/j.tafmec.2020.102473.

[5] V. Tamuzs, S. Tarasovs, U. Vilks, Delamination properties of translaminar-reinforced composites, Compos. Sci. Technol. 63 (10) (2003) 1423–1431, http://dx.doi.org/10.1016/S0266-3538(03)00042-3.

[6] M.J. Laffan, S.T. Pinho, P. Robinson, A.J. McMillan, Translaminar fracture toughness testing of composites: A review, Polym. Test. 31 (3) (2012) 481–489, http://dx.doi.org/10.1016/j.polymertesting.2012.01.002.

[7] Gianmaria Bullegas, Silvestre T. Pinho, Soraia Pimenta, Engineering the translaminar fracture behaviour of thin-ply composites, Compos. Sci. Technol. 131 (2016) 110–122, http://dx.doi.org/10.1016/j.compscitech.2016.06.002.

[8] Elham Moradi, Afshin Zeinedini, On the mixed mode I/II/III inter-laminar fracture toughness of cotton/epoxy laminated composites, Theor. Appl. Fract. Mech. 105 (November 2019) (2020) 102400, http://dx.doi.org/10.1016/j.tafmec.2019.102400.

[9] A. Turon, J. Costa, P.P. Camanho, C.G. Dávila, Simulation of delamination in composites under high-cycle fatigue, Compos. Part A: Appl. Sci. Manuf. 38 (11) (2007) 2270–2282, http://dx.doi.org/10.1016/j.compositesa.2006.11.009.

[10] C. Sarrado, A. Turon, J. Renart, I. Urresti, Assessment of energy dissipation during mixed-mode delamination growth using cohesive zone models, Compos. Part A: Appl. Sci. Manuf. 43 (11) (2012) 2128–2136, http://dx.doi.org/10.1016/j.compositesa.2012.07.009.

[11] Eghbal Jahanian, Afshin Zeinedini, Influence of drilling on mode II delamination of E-glass/epoxy laminated composites, Theor. Appl. Fract. Mech. 96 (April) (2018) 398–407, http://dx.doi.org/10.1016/j.tafmec.2018.06.002.

[12] Siroos Ahmadi, Afshin Zeinedini, Experimental, theoretical and numerical investigation of the drilling effects on mode I delamination of laminated composites, Aerosp. Sci. Technol. 104 (2020) 105992, http://dx.doi.org/10.1016/j.ast.2020.105992.

[13] J.J. van de Kerk, Rodolfo F.V. de Melo, Giovanni Bastiani, Mauricio Vicente Donadon, Mariano A. Arbelo, A numerical and experimental study of fasteners as a delamination arrest mechanism in composite laminates under mode I loading, Thin-Walled Struct. 191 (2023) 111047, http://dx.doi.org/10.1016/j.tws.2023.111047.

[14] M.L. Williams, On the stress distribution at the base of a stationary crack, J. Appl. Mech. 28 (1) (1961) 78–82, http://dx.doi.org/10.1115/1.3640470.

[15] F. Erdogan, G.C. Sih, On the crack extension in plates under plane loading and transverse shear, J. Fluids Eng. Trans. ASME 85 (4) (1963) 519–525, http://dx.doi.org/10.1115/1.3656897.

[16] J.G. Williams, P.D. Ewing, Fracture under complex stress - The angled crack problem, Int. J. Fract. 26 (4) (1984) 346–351, http://dx.doi.org/10.1007/BF00962967.

[17] Cheng Hou, Xiaochao Jin, Xueling Fan, Rong Xu, Zhiyong Wang, A generalized maximum energy release rate criterion for mixed mode fracture analysis of brittle and quasi-brittle materials, Theor. Appl. Fract. Mech. 100 (December 2018) (2019) 78–85, http://dx.doi.org/10.1016/j.tafmec.2018.12.015.

[18] Yanlin Wang, Weigang Wang, Bohua Zhang, Chun Qing Li, A review on mixed mode fracture of metals, Eng. Fract. Mech. 235 (June) (2020) 107126, http://dx.doi.org/10.1016/j.engfracmech.2020.107126.

[19] S.G. Lekhnitskii, Theory of Elasticity of an Anisotropic Body, first ed., MIR Publisher, Moscow, Russia, 1981, p. 431.

[20] G.C. Sih, P.C. Paris, G.R. Irwin, On cracks in rectilinearly anisotropic bodies, Int. J. Fract. Mech. 1 (3) (1965) 189–203, http://dx.doi.org/10.1007/BF00186854.

[21] M.B. Buczek, C.T. Herakovich, A normal stress criterion for crack extension direction in orthotropic composite materials, J. Compos. Mater. 19 (6) (1985) 544–553, http://dx.doi.org/10.1177/002199838501900606.

[22] M.A. Gregory, C.T. Herakovich, Predicting crack growth direction in unidirectional composites, J. Compos. Mater. 20 (1) (1986) 67–85, http://dx.doi.org/10.1177/002199838602000105.

[23] E.M. Wu, Application of fracture mechanics to anisotropic plates, J. Appl. Mech. 34 (4) (1967) 967–974, http://dx.doi.org/10.1115/1.3607864.

[24] C. Carloni, L. Nobile, Crack initiation behaviour of orthotropic solids as predicted by the strain energy density theory, Theor. Appl. Fract. Mech. 38 (2) (2002) 109–119, http://dx.doi.org/10.1016/S0167-8442(02)00089-7.

[25] C. Carloni, L. Nobile, Maximum circumferential stress criterion applied to orthotropic materials, Fatigue Fract. Eng. Mater. Struct. 28 (9) (2005) 825–833, http://dx.doi.org/10.1111/j.1460-2695.2005.00922.x.

[26] L.M.A. Cahill, S. Natarajan, S.P.A. Bordas, R.M. O'Higgins, C.T. McCarthy, An experimental/numerical investigation into the main driving force for crack propagation in uni-directional fibre-reinforced composite laminae, Compos. Struct. 107 (1) (2014) 119–130, http://dx.doi.org/10.1016/j.compstruct.2013.05.039.

[27] M. Arcan, Z. Hashin, A. Voloshin, A method to produce uniform plane-stress states with applications to fiber-reinforced materials - a specially designed specimen yields material properties under pure shear or uniform plane-stress conditions, Exp. Mech. 18 (4) (1978) 141–146, http://dx.doi.org/10.1007/BF02324146.

[28] ASTM, D7078 - Standard Test Method for Shear Properties of Composite Materials by V-Notched Rail, Standard, i, American Society for Testing Materials International, West Conshohocken, PA, 2012.

[29] R. Rikards, F.G. Buchholz, H. Wang, A.K. Bledzki, A. Korjakin, H.A. Richard, Investigation of mixed mode I/II interlaminar fracture toughness of laminated composites by using a CTS type specimen, Eng. Fract. Mech. 61 (3–4) (1998) 325–342, http://dx.doi.org/10.1016/S0013-7944(98)00068-X.

[30] J.Y. Cognard, L. Sohier, P. Davies, A modified arcan test to analyze the behavior of composites and their assemblies under out-of-plane loadings, Compos. Part A: Appl. Sci. Manuf. 42 (1) (2011) 111–121, http://dx.doi.org/10.1016/j.compositesa.2010.10.012.

[31] Dhatreyi Boyina, Anuradha Banerjee, R. Velmurugan, Mixed-mode translaminar fracture of plain-weave composites, Compos. Part B: Eng. 60 (2014) 21–28, http://dx.doi.org/10.1016/j.compositesb.2013.12.052.

[32] Leszek Malyszko, Andrzej Rutkiewicz, The shear behaviour of pine wood in the arcan test with the digital image correlation, in: S. Jemioło, A. Zbiciak, M. Mitew-Czajewska, M. Krzemiński, M. Gajewski (Eds.), MATEC Web Conf. 117 (January) (2017) 00113, http://dx.doi.org/10.1051/matecconf/201711700113.

[33] Khong Wui Gan, Tobias Laux, Siavash T. Taher, Janice M. Dulieu-Barton, Ole T. Thomsen, A novel fixture for determining the tension/compression-shear failure envelope of multidirectional composite laminates, Compos. Struct. 184 (October 2017) (2018) 662–673, http://dx.doi.org/10.1016/j.compstruct.2017.10.030.

[34] Israr Ud Din, Shanshan Tu, Pei Hao, Stéphane Panier, Kamran Ahmed Khan, Rehan Umer, S.Z.H. Shah, Gérald Franz, Muhammad Aamir, Sequential damage study induced in fiber reinforced composites by shear and tensile stress using a newly developed arcan fixture, J. Mater. Res. Technol. 9 (6) (2020) 13352–13364, http://dx.doi.org/10.1016/j.jmrt.2020.09.067.

[35] I. Ud Din, P. Hao, S. Panier, K.A. Khan, M. Aamir, G. Franz, K. Akhtar, Design of a new arcan fixture for in-plane pure shear and combined normal/shear stress characterization of fiber reinforced polymer composites, Exp. Tech. 44 (2) (2020) 231–240, http://dx.doi.org/10.1007/s40799-019-00353-9.

[36] Tobias Laux, Khong Wui Gan, Rodrigo P. Tavares, Carolina Furtado, Albertino Arteiro, Pedro P. Camanho, Ole T. Thomsen, Janice M. Dulieu-Barton, Modelling damage in multidirectional laminates subjected to multi-axial loading: Ply thickness effects and model assessment, Compos. Struct. 266 (2021) 113766, http://dx.doi.org/10.1016/j.compstruct.2021.113766.

[37] M.J. Laffan, S.T. Pinho, P. Robinson, Mixed-mode translaminar fracture of CFRP: Failure analysis and fractography, Compos. Struct. 95 (2013) 135–141, http://dx.doi.org/10.1016/j.compstruct.2012.06.012.

[38] H.A. Richard, K. Benitz, A loading device for the creation of mixed mode in fracture mechanics, Int. J. Fract. 22 (2) (1983) R55–R58, http://dx.doi.org/10.1007/BF00942726.

[39] J. Jamali, M.J. Mahmoodi, M.K. Hassanzadeh-Aghdam, J.T. Wood, A mechanistic criterion for the mixed-mode fracture of unidirectional polymer matrix composites, Compos. Part B: Eng. 176 (July) (2019) 107316, http://dx.doi.org/10.1016/j.compositesb.2019.107316.

[40] P. Hao, I. Ud Din, S. Panier, Development of modified arcan fixture for biaxial loading response of fiber-reinforced composites, Polym. Test. 80 (October) (2019) 106148.

[41] Hossein Taghibeigi, Afshin Zeinedini, Ahmed H. Oleiwi, On the mixed mode I/II translaminar fracture of plain-weave carbon, E-glass and kevlar reinforced laminated composites, Compos. Sci. Technol. 241 (2023) 110117, http://dx.doi.org/10.1016/j.compscitech.2023.110117.

[42] A. Zeinedini, M.H. Moradi, H. Taghibeigi, J. Jamali, On the mixed mode I/II/III translaminar fracture toughness of cotton/epoxy laminated composites, Theor. Appl. Fract. Mech. 109 (August) (2020) 102760, http://dx.doi.org/10.1016/j.tafmec.2020.102760.

[43] Abuzar Es'haghi Oskui, Nasser Soltani, Characterization of elastic-plastic fracture toughness of AM60 mg alloy under mixed-mode loading conditions, Eng. Fract. Mech. 204 (2018) 388–403.

[44] Abuzar Es'haghi Oskui, Mahmoud Ebrahimi, Shokouh Attarilar, Qudong Wang, Naghdali Choupani, Faramarz Djavanroodi, On the development of a testing device for fracture characterization under mixed-mode loading conditions, in: Advances in Accelerated Testing and Predictive Methods in Creep, Fatigue, and Environmental Cracking, American Society for Testing Materials International, West Conshohocken, PA, 2023, pp. 127–140.

[45] Francisco Maciel Monticeli, Felipe Ruivo Fuga, Maurício Vicente Donadon, A systematic review on translaminar fracture damage propagation in fiber-reinforced polymer composites, Thin-Walled Struct. 187 (November 2022) (2023) 110742, http://dx.doi.org/10.1016/j.tws.2023.110742.

[46] N. Zobeiry, R. Vaziri, A. Poursartip, Characterization of strain-softening behavior and failure mechanisms of composites under tension and compression, Compos. Part A: Appl. Sci. Manuf. 68 (2015) 29–41, http://dx.doi.org/10.1016/j.compositesa.2014.09.009.

[47] N. Blanco, D. Trias, S.T. Pinho, P. Robinson, Intralaminar fracture toughness characterisation of woven composite laminates. Part I: Design and analysis of a compact tension (CT) specimen, Eng. Fract. Mech. 131 (2014) 349–360, http://dx.doi.org/10.1016/j.engfracmech.2014.08.012.

[48] F. Cosmi, A. Bernasconi, Micro-CT investigation on fatigue damage evolution in short fibre reinforced polymers, Compos. Sci. Technol. 79 (2013) 70–76, http://dx.doi.org/10.1016/j.compscitech.2013.02.008.

[49] ASTM, E399 - test method for linear-elastic plane-strain fracture toughness of metallic materials, American Society for Testing Materials International, West Conshohocken, PA, 2013, pp. 1–33.

[50] Morteza Nejati, Saeid Ghouli, Majid R. Ayatollahi, Crack tip asymptotic fields in anisotropic planes: Importance of higher order terms, Appl. Math. Model. 91 (2021) 837–862, http://dx.doi.org/10.1016/j.apm.2020.09.025.

[51] S.V. Kamat, J.P. Hirth, Mixed mode I/II fracture toughness of 2034 aluminum alloys, Acta Mater. 44 (1) (1996) 201–208, http://dx.doi.org/10.1016/1359-6454(95)00169-8.

[52] J. Jamali, Y. Fan, J.T. Wood, The mixed-mode fracture behavior of epoxy by the compact tension shear test, Int. J. Adhes. Adhes. 63 (2015) 79–86, http://dx.doi.org/10.1016/j.ijadhadh.2015.08.006.

[53] J. Jamali, A-H.I. Mourad, Y. Fan, J.T. Wood, Through-thickness fracture behavior of unidirectional glass fibers/epoxy composites under various in-plane loading using the CTS test, Eng. Fract. Mech. 156 (2016) 83–95, http://dx.doi.org/10.1016/j.engfracmech.2016.01.016.

[54] Abbas Azhdari, Sia Nemat-Nasser, Energy-release rate and crack kinking in anisotropic brittle solids, J. Mech. Phys. Solids 44 (6) (1996) 929–951, http://dx.doi.org/10.1016/0022-5096(96)00012-9.

[55] C.T. Sun, Z.-H. Jin, Mixed mode fracture, in: Fracture Mechanics, vol. 4, Elsevier, 2012, pp. 105–121, http://dx.doi.org/10.1016/B978-0-12-385001-0.00005-5.

[56] Kaung Jain Chang, On the maximum strain criterion—a new approach to the angled crack problem, Eng. Fract. Mech. 14 (1) (1981) 107–124, http://dx.doi.org/10.1016/0013-7944(81)90021-7.

[57] R.J. Nuismer, An energy release rate criterion for mixed mode fracture, Int. J. Fract. 11 (2) (1975) 245–250, http://dx.doi.org/10.1007/BF00038891.

[58] C. Soutis, P.T. Curtis, A method for predicting the fracture toughness of CFRP laminates failing by fibre microbuckling, Compos. Part A: Appl. Sci. Manuf. 31 (7) (2000) 733–740, http://dx.doi.org/10.1016/S1359-835X(00)00003-8.

[59] C.F. Shih, B. Moran, T. Nakamura, Energy release rate along a three-dimensional crack front in a thermally stressed body, Int. J. Fract. 30 (1986) 79–102, http://dx.doi.org/10.1007/BF00034019.

[60] R.D. Henshell, K.G. Shaw, Crack tip finite elements are unnecessary, Internat. J. Numer. Methods Engrg. 9 (1975) 495–507, http://dx.doi.org/10.1002/nme.1620090302.

[61] Roshdy S. Barsoum, On the use of isoparametric finite elements in linear fracture mechanics, Internat. J. Numer. Methods Engrg. 10 (1976) 25–37, http://dx.doi.org/10.1002/nme.1620100103.

[62] G. Frossard, J. Cugnoni, T. Gmür, J. Botsis, Ply thickness dependence of the intralaminar fracture in thin-ply carbon-epoxy laminates, Compos. Part A: Appl. Sci. Manuf. 109 (2018) 95–104, http://dx.doi.org/10.1016/j.compositesa.2018.03.001.

[63] Felipe Ruivo Fuga, Maurício Vicente Donadon, Low velocity impact on pre-loaded composite plates: A novel standard-based experimental apparatus, Compos. Struct. 261 (2021) http://dx.doi.org/10.1016/j.compstruct.2020.113315.

[64] ASTM, D3039 - Standard Test Method for Tensile Properties of Polymer Matrix Composite Materials, Standard, American Society for Testing Materials International, West Conshohocken, PA, 2008.

[65] ASTM, D3518 - Standard Test Method for In-Plane Shear Response of Polymer Matrix Composite Materials by Tensile Test of a +-45° Laminate, Standard, 94, American Society for Testing Materials International, West Conshohocken, PA, 2007.

[66] H.A. Richard, SOME theoretical AND experimental ASPECTS OF MIXED MODE FRACTURES, in: Fracture 84, Elsevier, 1984, pp. 3337–3344, http://dx.doi.org/10.1016/B978-1-4832-8440-8.50358-6.

[67] Dhatreyi Boyina, T. Kirubakaran, Anuradha Banerjee, R. Velmurugan, Mixed-mode translaminar fracture of woven composites using a heterogeneous spring network, Mech. Mater. 91 (P1) (2015) 64–75, http://dx.doi.org/10.1016/j.mechmat.2015.07.013.

[68] Bruno Martins Leite, Luiz Fernando Martins Leite, Vitor Luiz Reis, Maurício Vicente Donadon, Nubia Nale Alves da Silveira, Strain rate effects on the intralaminar fracture toughness of composite laminates subjected to compressive load, Compos. Struct. 186 (2018) 94–105, http://dx.doi.org/10.1016/j.compstruct.2017.11.091.

[69] Rafael R.R. Souza, Sérgio L. Nascimento Junior, Núbia N.A. Silveira, Mariano A. Arbelo, Maurício V. Donadon, Translaminar fracture toughness and fatigue crack growth characterization of carbon-epoxy plain weave laminates, Polym. Compos. 40 (2019) 3791–3804, http://dx.doi.org/10.1002/pc.25247.

[70] Mahdi Fakoor, Mina S. Khezri, A micromechanical approach for mixed mode I/II failure assessment of cracked highly orthotropic materials such as wood, Theor. Appl. Fract. Mech. 109 (June) (2020) 102740, http://dx.doi.org/10.1016/j.tafmec.2020.102740.

[71] Zahra Khaji, Mahdi Fakoor, Strain energy release rate in combination with reinforcement isotropic solid model (SERIS): A new mixed-mode I/II criterion to investigate fracture behavior of orthotropic materials, Theor. Appl. Fract. Mech. 113 (March) (2021) 102962, http://dx.doi.org/10.1016/j.tafmec.2021.102962.